PERGAMON

International Journal of Solids and Structures 37 (2000) 7769–7786

INTERNATIONAL JOURNAL OF SOLIDS and STRUCTURES

www.elsevier.com/locate/ijsolstr

A phenomenological framework of constitutive modelling for incompressible and compressible elasto-plastic solids

C. Chen, T.J. Lu *

Department of Engineering, Cambridge University, Trumpington Street, Cambridge, CB2 1PZ, UK

Received 13 May 1999

Abstract

A unified framework of constructing phenomenological constitutive models for a broad class of elasto-plastic materials exhibiting either plastical incompressibility (e.g., grey cast iron) or plastical compressibility (e.g., metal foams) is proposed. The constitutive framework also enables the different yielding behaviours under tension and compression as well as differential hardening along different loading paths to be accounted for in a relatively simple manner. The resulting plasticity model does not require the difficult task of experimentally probing the initial yield surface and its subsequent evolution; it is completely determined from a set of as few as two distinctive stress–strain curves measured along the characteristic loading paths for isotropic materials. The predicted yielding behaviours for grey cast iron and metal foams compare favourably with those measured.

Keywords: Constitutive laws; Elastic-plastic solids; Cellular foams; Grey cast iron; Mises materials

1. Introduction

Classical constitutive models of phenomenological plasticity rely heavily on yield functions to distinguish plastic flow from reversible elastic deformation (Hill, 1994). Since the early isotropic models of Tresca and von Mises, there have been numerous attempts to construct empirical or conceptual yield functions suitable for modelling the elasto-plastic behaviours of a wide range of metal and non-metal materials (Drucker, 1948; Hill, 1950; Drucker and Prager, 1952; Bassani, 1977; Barlat et al., 1991; Takeda, 1993; Karafillis and Boyce, 1993; Hjelm, 1994). Often, these models require adequate experimental data on the initial and subsequent yield surfaces, which are not ordinarily available. Even when multiaxial tests are accessible, the determination of the initial yield surface and its subsequent evolution proves to be tedious, sometimes also ambiguous, for many materials of practical importance, due to the difficulty in distinguishing elastic deformation from plastic flow. Although a variety of methods (e.g., the off-set strain definition) have been proposed to separate plastic yielding from elastic regime, the shape of the resulting yield surface is found to be sensitive to the selected definition of yielding. Consequently, the yield surface is more or less determined at will. A convenient way to construct the yield function and the associated constitutive model based on

* Corresponding author. Tel.: +44-1223-766316; fax: +44-1223-332662.
E-mail address: tjl21@eng.cam.ac.uk (T.J. Lu).

0020-7683/00/$ - see front matter
PII: S0020-7683(00)00003-2

experimental information acquired from a few individual loading paths is thus desirable and perhaps more profitable.

Starting from the elastic complementary energy, two scalar measurements of stress and strain are introduced in this paper for isotropic materials. These are then used to construct a macroscopic stress potential which, together with the associated flow rule, characterises the elasto-plastic response of a solid material. Under loading, the model does not require that elastic deformation be separated from plastic yielding, whereas linear elasticity is assumed for unloading. The unknown material parameters in the model are determined by a set of characteristic multiaxial tests. Validation of the constitutive model is demonstrated for a plastically incompressible material, grey cast iron, and a compressible material, metallic foam, against available experimental measurements.

2. Theoretical framework

2.1. Characteristic stress and characteristic strain

Assume that the materials are initially isotropic and exhibit rate-independent response upon subsequent loading. Thus, when expressed in the principal coordinate system (x_1, x_2, x_3), Hook's law of linear elasticity is

$$\begin{Bmatrix} \varepsilon_1 \\ \varepsilon_2 \\ \varepsilon_3 \end{Bmatrix} = \frac{1}{E} \begin{bmatrix} 1 & -v & -v \\ -v & 1 & -v \\ -v & -v & 1 \end{bmatrix} \begin{Bmatrix} \sigma_1 \\ \sigma_2 \\ \sigma_2 \end{Bmatrix}, \tag{1}$$

where E and v are Young's modulus and Poisson's ratio of the material, and ε_i and $\sigma_i (i = 1, 2, 3)$ are the principal strains and stresses, respectively. For convenience, Eq. (1) can also be expressed as

$$\varepsilon_i = \frac{\partial W}{\partial \sigma_i}, \quad i = 1, 2, 3, \tag{2}$$

where the elastic complementary energy, W, when separated into the distortional and volumetric parts, is given by

$$W = \frac{1}{2\bar{E}} \left[\sigma_e^2 + \beta^2 \sigma_m^2 \right]. \tag{3}$$

Here, σ_e and σ_m are the Mises effective stress and mean stress, respectively,

$$\begin{aligned} \sigma_e &= \sqrt{\tfrac{1}{2}\left[(\sigma_1 - \sigma_2)^2 + (\sigma_2 - \sigma_3)^2 + (\sigma_3 - \sigma_1)^2 \right]}, \\ \sigma_m &= \frac{\sigma_1 + \sigma_2 + \sigma_3}{3}, \end{aligned} \tag{4}$$

whilst $\bar{E}$ and β are material constants defined by

$$\bar{E} = \frac{3E}{2(1+v)}, \qquad \beta^2 = \frac{9(1-2v)}{2(1+v)}. \tag{5}$$

From Eq. (3), a scalar measure of stresses, $\bar{\sigma}$, can be introduced as

$$\bar{\sigma}^2 = \sigma_e^2 + \beta^2 \sigma_m^2, \tag{6}$$

which has a work conjugate, $\bar{\varepsilon}$, given by

$$\bar{\varepsilon}^2 = \varepsilon_e^2 + \frac{\varepsilon_v^2}{\beta^2}, \tag{7}$$

where the effective strain ε_e and volumetric strain ε_v are separately the work conjugates of σ_e and σ_m. In terms of principal strains, these are

$$\varepsilon_e = \sqrt{\frac{2}{9}\left[(\varepsilon_1-\varepsilon_2)^2+(\varepsilon_2-\varepsilon_3)^2+(\varepsilon_3-\varepsilon_1)^2\right]}, \qquad \varepsilon_v = \varepsilon_1+\varepsilon_2+\varepsilon_3. \tag{8}$$

In the remainder of this paper, $\bar{\sigma}$ and $\bar{\varepsilon}$ are termed characteristic stress and characteristic strain, respectively. It can be easily verified that $\bar{\sigma}$ is related to $\bar{\varepsilon}$ by

$$\bar{\sigma} = \bar{E}\bar{\varepsilon}, \tag{9}$$

where $\bar{E}$ is the generalised Young's modulus defined in Eq. (5). Under hydrostatic loading, uniaxial loading or simple shear, the expressions for $\bar{\sigma}$ and $\bar{\varepsilon}$ reduce to

$$\bar{\sigma} = \beta|\sigma_h|, \qquad \bar{\varepsilon} = \frac{|\varepsilon_h|}{\beta}, \tag{10}$$

$$\bar{\sigma} = \frac{1}{3}\sqrt{9+\beta^2}|\sigma_u|, \qquad \bar{\varepsilon} = \frac{3|\varepsilon_u|}{\sqrt{9+\beta^2}}, \tag{11}$$

$$\bar{\sigma} = \sqrt{3}|\tau|, \qquad \bar{\varepsilon} = \frac{\sqrt{3}}{3}|\gamma|, \tag{12}$$

where σ_h and ε_h are the mean stress and volumetric strain under hydrostatic loading, σ_u and ε_u are the uniaxial stress and strain under uniaxial loading, and τ are γ are the shear stress and engineering shear strain in simple shear. Deshpande and Fleck (1999) used a slightly different definition of $\bar{\sigma}$ and $\bar{\varepsilon}$ to study the yielding of metallic foams. In Deshpande and Fleck (1999), the characteristic strain is defined in terms of plastic strain instead of the total strain as in Eq. (7); also, β is defined by using the plastic Poisson's ratio v_p instead of the elastic Poisson's ratio v as in Eq. (5). Since v_p by definition is the absolute value of the ratio of transverse to longitudinal plastic strain under uniaxial loading, it can vary with the plastic deformation – careful experiments need to be performed to measure its value.

The discussion hitherto has been limited to linear elasticity and it is shown that the macroscopic response behaviours of an elastically deforming isotropic material subjected to arbitrary external loading are fully characterised by characteristic stress $\bar{\sigma}$, characteristic strain $\bar{\varepsilon}$ and generalised Young's modulus $\bar{E}$. For a plastically deforming material, it is *proposed* here that $\bar{\sigma}$ and $\bar{\varepsilon}$ are continuously used to characterise its elasto-plastic response. As an illustration, Fig. 1 plots typical $\bar{\sigma}$ versus $\bar{\varepsilon}$ curves of the material under three distinctive loading paths: *a* corresponds to the softest loading path, *c* is the hardest path, and *b* is an intermediate path. (For plastically incompressible materials such as grey cast iron, path *c* becomes the hydrostatic loading as represented by the broken line in Fig. 1.) The corresponding elastic limit points along paths *a*, *b* and *c* are denoted by points 1, 2 and 3. In the elastic region, i.e., between points 0 and 1, the $\bar{\sigma}$–$\bar{\varepsilon}$ curves collapse into a single straight line with a slope, $\bar{E}$. If the variation of the $\bar{\sigma}$–$\bar{\varepsilon}$ curves along different loading paths is also small in the plastic regime for the isotropic materials to be considered, there would be no major difficulty in determining the initial yield surface and its subsequent evolution. Unfortunately, for most engineering materials, both the elastic limit point and the post yielding behaviour differ, often significantly, when the loading path is changed. It then becomes much more difficult to determine an adequate initial yield surface, let alone its evolution. An alternative approach to avoid such difficulties is desirable and is introduced below.

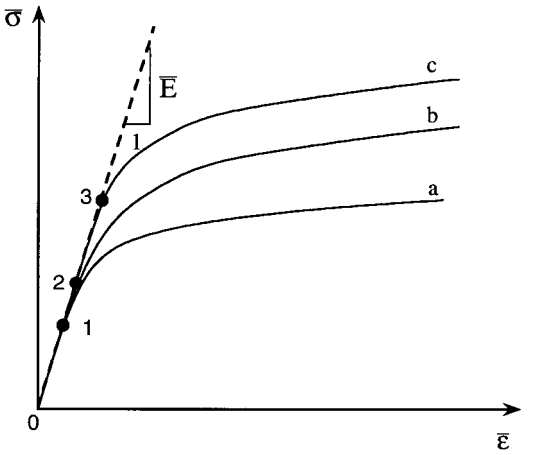

Fig. 1. Stress versus strain curves along typical loading paths in the $\bar{\sigma}$–$\bar{\varepsilon}$ space. For incompressible solids, hydrostatic loading is represented by the broken line with slope $\bar{E}$.

2.2. Stress potential and constitutive law

Inspired by the modified Mises yield function of Drucker and Prager (1952), the following 'yield' function is proposed

$$\Phi = \bar{\sigma}^2 + \Phi_1(\bar{\varepsilon}, \sigma_{ij}) - Y(\bar{\varepsilon}) = 0, \tag{13}$$

where σ_{ij} is the stress tensor and $\Phi_1(\bar{\varepsilon}, \sigma_{ij})$ and $Y(\bar{\varepsilon})$ are the material parameters to be determined from experiments. For isotropic materials, Φ_1 is in general dependent upon the mean stress σ_m, the effective stress σ_e and the third deviatoric stress invariant J_3. For simplicity, it is assumed here that the effects of σ_e and J_3 on Φ_1 are negligible. Thence,

$$\Phi_1 = \Phi_1(\bar{\varepsilon}, \sigma_m). \tag{14}$$

Further, once Φ_1 and Y are determined, it is assumed that Eq. (13) can be used in conjunction with the associated flow rule to give the *total* strain rate as

$$\dot{\varepsilon}_{ij} = \dot{\lambda}\frac{\partial \Phi}{\sigma_{ij}}, \tag{15}$$

where the proportionality factor $\dot{\lambda}$ is determined from the consistence condition of plasticity as

$$\dot{\Phi} = \frac{\partial \Phi}{\partial \sigma_{ij}}\dot{\sigma}_{ij} + \frac{\partial \Phi}{\partial \bar{\varepsilon}}\dot{\bar{\varepsilon}} = 0. \tag{16}$$

Note that, in classical plasticity, the total strain rate ε_{ij} in Eq. (15) is replaced by the plastic strain rate ε^p_{ij}, so that Φ is a plastic flow potential. The reason of adopting the total strain rate in Eq. (15) is that, in doing so, elastic deformation can also be modelled by Eqs. (13) and (15). In fact, as $\bar{\sigma} = \bar{E}\bar{\varepsilon}$ in the elastic regime, it follows from Eq. (13) that $\Phi_1 = 0$ and $Y(\bar{\varepsilon}) = \bar{E}^2\bar{\varepsilon}^2$. As a result, Eq. (13) together with Eqs. (15) and (16) reproduce the linear elastic constitutive law. Consequently, in the present framework, it is assumed that there is no need to distinguish elastic deformation from plastic deformation in Eqs. (13) and (15) – the daunting task of determining the initial yield surface and its evolution is therefore avoided. Although Eq. (13) appears to resemble the modified Mises yield function, there exists a notable difference between the two models. Strictly speaking, Φ in Eq. (13) differs from the conventional yield function. In the present model,

the Mises effective stress is replaced by the characteristic stress $\bar{\sigma}$, and the effective plastic strain is replaced by the characteristic strain $\bar{\varepsilon}$; both elastic and plastic deformations can be described by Eqs. (13) and (15). Therefore, even though two fundamental elements of classical plasticity, namely, the associated flow rule and the consistence condition, are applied to construct the constitutive law from Eq. (13), Φ will be termed a stress potential instead of yield function in the following sections. Finally, and importantly, if elastic deformation is negligibly small compared to plastic deformation, i.e., $\varepsilon_{ij}^{\mathrm{p}} \cong \varepsilon_{ij}$, Eqs. (15) and (16) reduce to those in classical plasticity.

2.3. Application to Mises materials

Before validating the proposed constitutive law with practical materials, an interesting model material, namely, the Mises material, is first examined. Here, Mises materials refer to a class of materials, the yielding of which is dictated by the Mises criterion. It will be shown that the ever popular Mises model for plastically incompressible materials can be well approximated by the present model, where no constraint on plastical incompressibility is imposed. Since there is no difference between tensile and compressive behaviour for Mises materials, it is assumed here that

$$\Phi_1 = A(\bar{\varepsilon})\sigma_{\mathrm{m}}^2. \tag{17}$$

The stress potential Eq. (13) then becomes

$$\Phi = \bar{\sigma}^2 + A(\bar{\varepsilon})\sigma_{\mathrm{m}}^2 - Y(\bar{\varepsilon}) = 0, \tag{18}$$

where $A(\bar{\varepsilon})$ and $Y(\bar{\varepsilon})$ are two material parameters. Theoretically, stress versus strain curves along any two distinctive loading paths can be used to evaluate $A(\bar{\varepsilon})$ and $Y(\bar{\varepsilon})$. In order to increase the predicative power of the constitutive model, however, it is suggested to follow characteristic loading paths (e.g., hydrostatic loading together with simple shear or uniaxial stressing). Hydrostatic and simple shear stress–strain curves are used below.

Consider the Ramberg–Osgood model for a Mises material,

$$\frac{E\varepsilon_{ij}}{\sigma_0} = (1+\nu)\frac{s_{ij}}{\sigma_0} + (1-2\nu)\frac{\sigma_{\mathrm{m}}}{\sigma_0}\delta_{ij} + \frac{3\alpha}{2}\left(\frac{\sigma_{\mathrm{e}}}{\sigma_0}\right)^{n-1}\frac{s_{ij}}{\sigma_0}, \tag{19}$$

where ε_{ij} is the strain tensor, δ_{ij} is the Kronecker delta, $s_{ij} = \sigma_{ij} - \delta_{ij}\sigma_{\mathrm{m}}$ is the deviatoric stress tensor, σ_0 is a reference yield stress, and α and n are material constants. Under simple shear, Eq. (19) simplifies to

$$\frac{E\varepsilon_{12}}{\sigma_0} = (1+\nu)\frac{\sigma_{12}}{\sigma_0} + \frac{\sqrt{3}\alpha}{2}\left(\frac{\sqrt{3}\sigma_{12}}{\sigma_0}\right)^n. \tag{20}$$

With $\gamma = 2\varepsilon_{12}$, $\tau = \sigma_{12}$ and the characteristic stress and strain given by Eq. (12), Eq. (20) can be rewritten as

$$\frac{\bar{E}\bar{\varepsilon}}{\sigma_0} = \frac{\bar{\sigma}_{\mathrm{s}}}{\sigma_0} + \frac{3\alpha}{2(1+\nu)}\left(\frac{\bar{\sigma}_{\mathrm{s}}}{\sigma_0}\right)^n, \tag{21}$$

where the subscript 's' is used to denote simple shear. On the contrary, the hydrostatic behaviour of a plastically incompressible Mises material is governed by linear elasticity, i.e.,

$$\sigma_{\mathrm{h}} = \kappa\varepsilon_{\mathrm{h}}, \tag{22}$$

where $\kappa = \bar{E}/\beta^2$ is the bulk modulus and the subscript 'h' denotes hydrostatic loading. In view of Eq. (10), this can be rearranged as

$$\bar{\sigma}_{\mathrm{h}} = \bar{E}\bar{\varepsilon}, \tag{23}$$

which corresponds to the broken line in Fig. 1. Finally, the two material parameters $Y(\bar{\varepsilon})$ and $A(\bar{\varepsilon})$ in Eq. (18), when determined from the simple shear and hydrostatic stress–strain curves, have the form

$$Y(\bar{\varepsilon}) = \bar{\sigma}_s^2, \qquad A(\bar{\varepsilon}) = \beta^2 \frac{\bar{\sigma}_s^2 - \bar{\sigma}_h^2}{\bar{\sigma}_h^2}, \tag{24}$$

where $\bar{\sigma}_h$ is related to $\bar{\varepsilon}$ through Eq. (23) and the dependence of $\bar{\sigma}_s$ on $\bar{\varepsilon}$ is determined by solving the non-linear equation (21). Therefore, the highly non-linear behaviour represented by Eq. (21) is implicitly incorporated into the present model through $A(\bar{\varepsilon})$ and $Y(\bar{\varepsilon})$ in Eq. (24).

The stress potential (18) is now complete; together with Eqs. (15) and (16), it characterises the elasto-plastic behaviours of a Mises material governed by the Ramberg–Osgood model. In general, numerical procedures are needed to integrate Eq. (15) to obtain the stress–strain curves along various deformation paths. As an illustration, consider the following proportional axisymmetric loading path:

$$\sigma_{11} = \sigma_{22} = \sigma, \quad \sigma_{33} = x\sigma, \quad \sigma_{12} = \sigma_{23} = \sigma_{31} = 0 \quad (x \geqslant 1), \tag{25}$$

where σ and x are constants, with $x \to \infty$ representing uniaxial stressing. For this particular loading path, the $\bar{\sigma}$–$\bar{\varepsilon}$ curve can be obtained in closed form as

$$\bar{\sigma} = \bar{\sigma}_s \Bigg/ \sqrt{1 + \beta^2 \frac{(\bar{\sigma}_s^2 - \bar{\sigma}_h^2)(2+x)^2}{\bar{\sigma}_h^2[9(1-x)^2 + \beta^2(2+x)^2]}} \tag{26}$$

for the present model and

$$\frac{\bar{E}\bar{\varepsilon}}{\sigma_0} = \sqrt{\left[(x-1)\Sigma + \alpha\frac{3(x-1)^n}{2(1+\nu)}\Sigma^n\right]^2 + \frac{1}{\beta^2}\left[\frac{3(1-2\nu)}{2(1+\nu)}(2+x)\Sigma\right]^2}, \tag{27}$$

$$\Sigma = \frac{\bar{\sigma}/\sigma_0}{\sqrt{(x-1)^2 + \beta^2\frac{(2+x)^2}{9}}}$$

for the Ramberg–Osgood model. Notice that, as only the simple shear and the hydrostatic loading behaviours given by the Ramberg–Osgood model are used to characterise the present model in Eq. (26), it is not surprising that both models, i.e., Eqs. (26) and (27), would yield identical predictions under simple shear and hydrostatic loading (shown as solid lines in Fig. 2). In order to further verify the present model, comparisons between the predictions by the present model and by the Ramberg–Osgood model along other loading paths are made. Only the stress–strain curves along the three selected loading paths (i.e., $x = 2, 4, \infty$ in Eq. (25)) are presented, as results along other loading paths exhibit similar trends. It should be noted that $x = \infty$ represents the uniaxial loading path. The $\bar{\sigma}$ versus $\bar{\varepsilon}$ curves predicted from Eq. (26) are compared with those calculated directly from the Ramberg–Osgood model (i.e., Eq. (27)) in Fig. 2a for the case of strong hardening ($n = 2$) and in Fig. 2b for the case of weak hardening ($n = 10$). Other material constants used in the plotting are $\nu = 0.3$ and $\alpha = 3/7$. In Fig. 2, symbols denote results from the Ramberg–Osgood model, whereas the various dotted and dashed lines refer to those obtained from the present model. Close agreement between the present model and the Ramberg–Osgood model is obtained, especially at large strain levels. When the strains are large, $\bar{\sigma}_h \gg \bar{\sigma}_s$ and $A(\bar{\varepsilon}) \to -\beta^2$ according to Eq. (24), and hence the stress potential (18) approaches the limit:

$$\Phi = \sigma_e^2 - Y(\bar{\varepsilon}) = 0. \tag{28}$$

Also, at high strain levels, the elastic deformation is usually negligible so that the elastic Poisson's ratio ν may be replaced by the plastic Poisson's ratio ν_p. As $\nu_p = 1/2$ for Mises materials, it follows that $\bar{\sigma} \to \sigma_e$

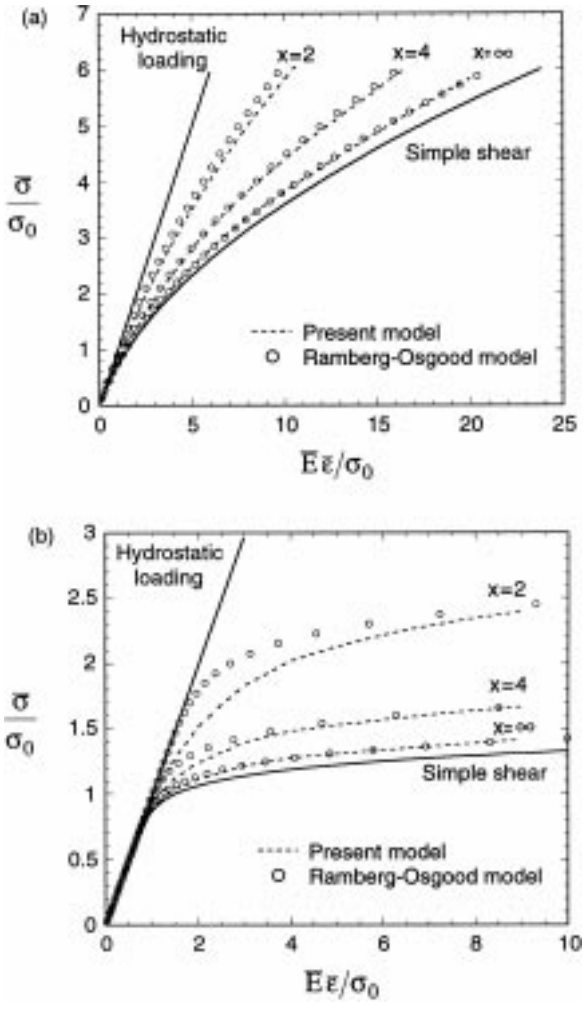

Fig. 2. Comparison of $\bar{\sigma}$–$\bar{\varepsilon}$ curves predicted by the present model and the Ramberg–Osgood model for Mises materials subjected to various proportional loading paths: (a) $\alpha = 3/7, \nu = 0.3, n = 2$; (b) $\alpha = 3/7, \nu = 0.3, n = 10$.

and $\bar{\varepsilon} \to \varepsilon_e$. Thus, at high strain levels, Mises materials can be well described by the proposed constitutive model.

3. Validation of model

Although there exist ample experimental data on the yielding of engineering materials (see, for example, the review article of Hecker, 1975), most were reported in terms of the initial yield surface and its evolution. Few of them are presented using stress–strain curves along different loading paths to allow for the calibration of the stress potential (13) and validation of the resulting constitutive model. Fortunately, careful experimental and theoretical studies have been conducted by Hjelm (1994) for a plastically incompressible material, grey cast iron, and by Deshpande and Fleck (1999) for one type of plastically compressible

materials, metal foams. The experimental data provided are sufficient to characterise and validate the proposed constitutive model, as demonstrated below.

3.1. Grey cast iron

The yielding of grey cast iron is complicated due to the graphite flakes distributed in the steel matrix (Coffin, 1950; Hjelm, 1994). In tension, grey cast iron exhibits brittle behaviour and yields according to the maximum principal stress criterion which is attributed to the stress concentrations caused by the graphite flakes; its volume increases as a result of the graphite flakes being opened up. In compression, the macroscopic yield response of grey cast iron is dominated by the steel matrix, hence governed by the Mises criterion, with a yield limit three or more times higher than that in tension; also, strain hardening under compression is much stronger than that under tension. Hjelm (1994) proposed a composite yield surface to describe the different yield behaviours in tension and compression, with tensile yielding governed by the maximum principal stress and compressive yielding by the Mises effective stress. Non-associated flow rule is suggested by Hjelm (1994) to avoid the corners on the yield surface in the tensile region, with the flow potential consisting of the Mises cylinder in compression and the Rankine cube in tension when plotted in the principal stress plane. A differential hardening model is proposed to characterise the hardening behaviour, with the assumption that the graphite flakes do not influence hardening in compression and that tensile hardening is controlled separately by the volumetric plastic strain (corresponding to the opening up of the graphite flakes) and the deviatoric volumetric plastic strain (corresponding to inelastic shearing of the matrix). This rather complicated constitutive model has been implemented into the finite element code ABAQUS where it is termed the cast iron model. Hjelm (1994) compared the model predictions to those measured from biaxial tests using thin cruciform specimens. A set of 10 stress–strain curves are measured along the compression–compression, tension–tension, compression–tension and tension–compression biaxial loading paths; a reasonable agreement between theory and experiment is obtained.

Because the out of plane behaviours of grey cast iron are not reported by Hjelm (1994), only its in-plane behaviours will be studied below to validate the present model. A plane stress assumption could be made to investigate the in-plane behaviour. However, in the present paper, due to the lack of test data on the out of plane deformation in either plane stress or plane strain for grey cast iron, a two-dimensional version of the three-dimensional constitutive model proposed in Section 2 is employed, where only the in-plane behaviour of grey cast iron is accounted for. Such a two-dimensional constitutive model has been found to be useful in studying the elasto-plastic yielding of some two-dimensional model materials, e.g., honeycombs and 2D cellular materials (cf. Warren and Kraynik, 1987; Chen et al., 1999). A two-dimensional version of the full three-dimensional model can be developed by following the same procedures leading to Eqs. (2)–(12), except that Hook's law of Eq. (1) should be replaced by

$$\begin{Bmatrix} \varepsilon_1 \\ \varepsilon_2 \end{Bmatrix} = \frac{1}{E} \begin{bmatrix} 1 & -v \\ -v & v \end{bmatrix} \begin{Bmatrix} \sigma_1 \\ \sigma_2 \end{Bmatrix}. \tag{29}$$

Accordingly, only a few changes need to be made. Specifically, σ_e and σ_m in Eq. (4), $\bar{E}$ and β in Eq. (5), and ε_e and ε_v in Eq. (8) now read

$$\sigma_e = |\sigma_1 - \sigma_2|, \qquad \sigma_m = \frac{\sigma_1 + \sigma_2}{2}, \tag{30}$$

$$\bar{E} = \frac{2E}{1+v}, \qquad \beta^2 = \frac{4(1-v)}{1+v}, \tag{31}$$

$$\varepsilon_e = \frac{|\varepsilon_1 - \varepsilon_2|}{2}, \qquad \varepsilon_v = \varepsilon_1 + \varepsilon_2. \tag{32}$$

Also, Eq. (11) for uniaxial loading is changed to

$$\bar{\sigma} = \frac{1}{2}\sqrt{4+\beta^2}|\sigma_u|, \qquad \bar{\varepsilon} = \frac{2\varepsilon_u}{\sqrt{4+\beta^2}}. \tag{33}$$

Notice that σ_e and σ_m given by Eq. (30) are two stress invariants in the σ_1–σ_2 space, which are different from the von Mises effective stress and mean stress under the condition of plane stress. Also, note that the two-dimensional definitions of Eqs. (29)–(32) for grey cast iron should not be employed to study the metallic foams considered in the Section 3.2, where the three-dimensional model is more appropriate.

To model the differential deformation behaviours of cast iron in tension and in compression, the stress potential of Eq. (13) is taken as

$$\Phi = \bar{\sigma}^2 + B(\bar{\varepsilon})\sigma_m - Y(\bar{\varepsilon}) = 0, \tag{34}$$

where the material properties $B(\bar{\varepsilon})$ and $Y(\bar{\varepsilon})$ are to be determined by two characteristic tests. Amongst the 10 multiaxial loading tests conducted by Hjelm (1994), stress versus strain curves along five different loading paths are presented which can be used to calibrate the stress potential (34). Typical characteristic tests are uniaxial tension and equibiaxial tension together with uniaxial compression and equibiaxial compression, although Hjelm (1994) only reported the stress–strain curves under uniaxial tension and equibiaxial tension. Because the reported strain level of the equibiaxial tension test ($\sigma_1/\sigma_2 = 1$) is too small (about 0.14%), it is not taken as a characteristic test. Instead, uniaxial tension together with a nearly equibiaxial compression test ($\sigma_1/\sigma_2 = 3/2$), of which Hjelm (1994) reported the only available stress–strain curve in the compression–compression quadrant, are used to determine $B(\bar{\varepsilon})$ and $Y(\bar{\varepsilon})$. The corresponding $\bar{\sigma}$–$\bar{\varepsilon}$ curves for the two characteristic tests are shown in Fig. 3. Since $E = 126$ GPa and $\nu = 0.265$ for cast iron, it follows from Eq. (31) that $\bar{E} = 199.2$ GPa and $\beta = 1.525$. In Fig. 3, symbols denote the experimental data extracted from Hjelm (1994) whereas solid lines represent the fitted results, given by

$$\begin{aligned} \bar{\sigma}_{cc} &= 199.2\bar{\varepsilon} + 6.678\bar{\varepsilon}^2 - 4.740\bar{\varepsilon}^3 \\ \bar{\sigma}_{ut} &= 199.2\bar{\varepsilon} - 24.20\bar{\varepsilon}^2 - 2.628\bar{\varepsilon}^3 \end{aligned} \quad (0 < \bar{\varepsilon} < 0.3\%), \tag{35}$$

where the units for the characteristic stress and strain are MPa and microstrain, respectively, and the subscripts 'cc' and 'ut' refer to compression–compression and uniaxial tension, respectively. Finally, the two

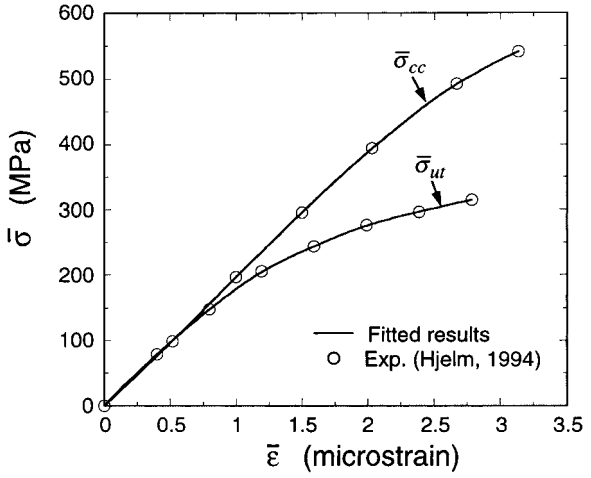

Fig. 3. Characteristic $\bar{\sigma}$–$\bar{\varepsilon}$ curves for characterising the constitutive model of grey cast iron.

material properties in Eq. (34) are determined from the characteristic stress–strain curves subjected to uniaxial tension and compression–compression loading as

$$B(\bar{\varepsilon}) = -\frac{\bar{\sigma}_{ut}^2 - \bar{\sigma}_{cc}^2}{\bar{\sigma}_{ut}\Big/\sqrt{4+\beta^2} + \bar{\sigma}_{cc}\Big/\sqrt{4/25+\beta^2}},$$
$$Y(\bar{\varepsilon}) = \bar{\sigma}_{ut}\bar{\sigma}_{cc}\frac{\bar{\sigma}_{ut}\Big/\sqrt{4/25+\beta^2} + \bar{\sigma}_{cc}\Big/\sqrt{4+\beta^2}}{\bar{\sigma}_{ut}\Big/\sqrt{4+\beta^2} + \bar{\sigma}_{cc}\Big/\sqrt{4/25+\beta^2}}. \tag{36}$$

The stress potential (34) can now be used in conjunction with the associated flow rule (15) to predict the deformation behaviour along arbitrary monotonic loading paths. Contours of the stress potential are plotted in Fig. 4 in the σ_1–σ_2 space for selected levels of the characteristic strain $\bar{\varepsilon}$. At low strain levels (i.e., $\bar{\varepsilon} < 0.08\%$), the stress potential expands in a self-similar manner and is governed by elastic deformation. Upon further straining into the plastic regime, it gradually translates from the origin towards the compression–compression quadrant, as there is stronger hardening in compression than that in tension. The predicted stress–strain curves along five different monotonic loading paths are presented in Fig. 5 as solid lines and compared with those measured by Hjelm (1994). (Because linear elasticity is assumed for unloading in the present model, the unloading stress–strain curves are not included in Fig. 5.) In all cases, the model predictions compare favourably with experimental measurements. Since uniaxial tension and compression–compression results have been used to calibrate the model, the close agreement between prediction and test data is therefore expected (Fig. 5a and b). However, the close agreement observed along three other biaxial loading tests, i.e., $\sigma_1/\sigma_2 = 1$ (Fig. 5c), $\sigma_1/\sigma_2 = -2$ (Fig. 5d) and $\sigma_1/\sigma_2 = -1/2$ (Fig. 5e), serve to validate the present constitutive model.

According to Hjelm (1994), a Mises yield function together with an associated flow rule yields quite satisfactory predictions for cast iron under compression; in tension, however, a modified Mises model is

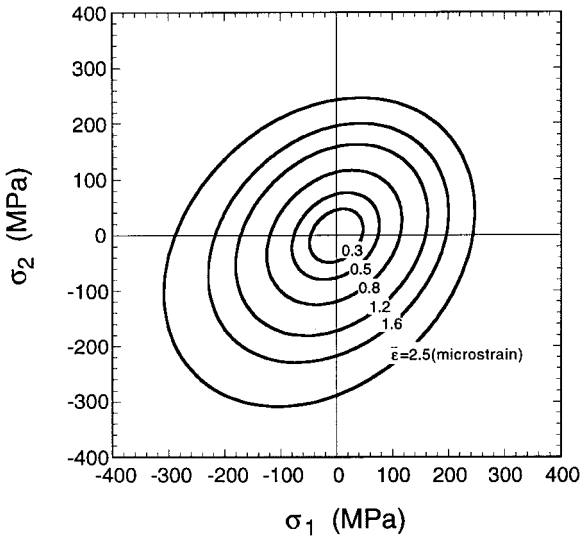

Fig. 4. Stress potential contours at selected characteristic strain levels for grey cast iron.

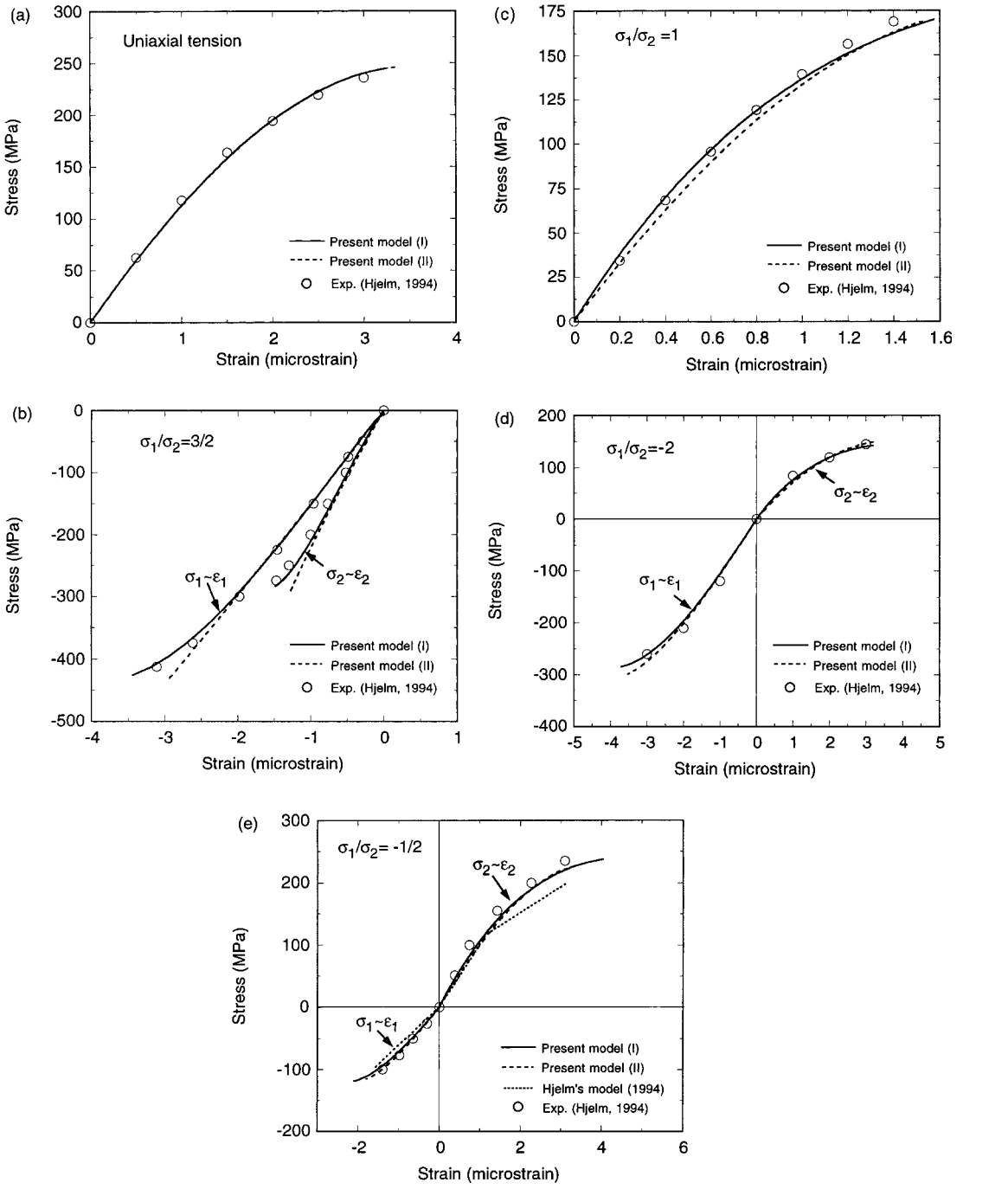

Fig. 5. Comparison between predicted and experimentally measured stress versus strain curves of grey cast iron along various proportional loading paths: (a) uniaxial tension, (b) compression–compression ($\sigma_1/\sigma_2 = 3/2$), (c) equibiaxial tension ($\sigma_1/\sigma_2 = 1$), (d) tension–compression ($\sigma_1/\sigma_2 = -2$), (e) compression–tension ($\sigma_1/\sigma_2 = -1/2$).

needed to account for the volumetric changes due to the opening up of graphite flakes. The resulting yield function is

$$\Phi^* = \begin{cases} \frac{1}{3}q^2 + p(\sigma_C - \sigma_T) - \frac{1}{3}\sigma_C\sigma_T, & p > -\sigma_C, \\ \frac{1}{3}(q^2 - \sigma_C^2), & p \leqslant -\sigma_C, \end{cases} \tag{37}$$

where q is the von Mises effective stress, p is the mean stress, and σ_T and σ_C are the yield limits in uniaxial tension and uniaxial compression, respectively. It should be noted that neither the Mises model nor the modified one is capable of modelling, the yielding behaviours of cast iron under both tensile and compressive loadings: the Mises model overestimates the tensile behaviour, whereas the modified Mises model overestimates the compressive response. The predicted stress–strain curve by using Hjelm's model for the specific loading path $\sigma_1/\sigma_2 = -1/2$ is shown in Fig. 5e as dotted lines. It is seen that the simple stress potential (34) yields more accurate predictions than those from Eq. (37) when compared with experimental measurements. More importantly, the differential yielding behaviours of cast iron in tension and compression can be modelled sufficiently accurately by the present model using a single stress potential.

It is seen from Fig. 3 that, along the nearly equibiaxial compression loading path, the characteristic stress varies almost linearly with the characteristic strain. As discussed earlier, this is attributed to the fact that grey cast iron is nearly plastically incompressible. Consequently, we can assume that grey cast iron under equal biaxial compression is plastically incompressible, which can be mathematically expressed as $\bar{\sigma}_{hc} = \bar{E}\bar{\varepsilon}$, where subscript 'hc' denotes the characteristic stress under equibiaxial compression. Due to the incompressibility assumption, only one additional test is needed to evaluate the material parameters $B(\bar{\varepsilon})$ and $Y(\bar{\varepsilon})$ in the stress potential (34). Here, the simplest uniaxial tension test is taken as the additional test. The resulting $B(\bar{\varepsilon})$ and $Y(\bar{\varepsilon})$ now have the form of

$$\begin{aligned} B(\bar{\varepsilon}) &= -\frac{\bar{\sigma}_{ut}^2 - \bar{\sigma}_{hc}^2}{\bar{\sigma}_{ut}\Big/\sqrt{4+\beta^2} + \bar{\sigma}_{hc}/\beta}, \\ Y(\bar{\varepsilon}) &= \bar{\sigma}_{ut}\bar{\sigma}_{hc}\frac{\bar{\sigma}_{ut}/\beta + \bar{\sigma}_{hc}\Big/\sqrt{4+\beta^2}}{\bar{\sigma}_{ut}\Big/\sqrt{4+\beta^2} + \bar{\sigma}_{hc}/\beta}. \end{aligned} \tag{38}$$

The predicted stress–strain curves from Eqs. (15), (34) and (38) are included in Fig. 5 as dashed lines and are labelled 'model II', as opposed to those from 'model I' based on the calibrations of Eq. (36). Except at relatively large strains in the nearly equal biaxial compression test ($\sigma_1/\sigma_2 = 3/2$, Fig. 5b), the simplified model is seen to work fairly well. The slight deviation of the stress–strain curve from linearity in Fig. 5b indicates that plastic incompressibility is perhaps not a good assumption for grey cast iron at small strain levels. However, at relatively large strains, the graphite flakes may be crushed and hence may become incompressible.

3.2. Metallic foams

Low-density cellular metals (foams) are a new class of engineering materials with promising mechanical, thermal, electrical and acoustical properties. Their elastic and plastic properties have been studied extensively (Gibson and Ashby, 1997; Ashby et al., 1998). In general, the yielding of a foam material is strongly pressure sensitive, and is different in tension and compression. Due to the lack of detailed experimental data

in multiaxial tension and the fact that foams are usually applied as compression structures, the focus below will be directed on compression.

Using a mechanism-based micromechanics model for open-celled rigid polymeric foams, Gibson et al. (1989) derived a yield surface

$$\frac{\sigma_e}{\sigma_s} = \pm\lambda\rho^{-3/2}\left[1 - \left(\frac{3\sigma_m}{\sigma_s\rho}\right)^2\right], \tag{39}$$

where σ_s is the yield strength of the cell wall material, λ is a material constant to be evaluated by uniaxial loading, and ρ is the relative density of the foam. Note that this yield surface may be truncated by elastic buckling in compression and by brittle fracture in tension, depending upon the stress state and the microstructures of the foam. Due to the complicated failure mechanisms associated with the irregular and imperfection-prone microstructures commonly found in foams, it is difficult to derive user-friendly yield functions from micromechanics study. A phenomenological approach has therefore been widely applied to formulate the constitutive model for both polymeric and metallic foams. The analytical results of Gibson et al. (1989) are fitted by Puso and Govindjee (1995) with a single elliptical yield surface given, in the σ_e–σ_m space, by

$$\sigma_e^2 + \frac{1}{R}\sigma_m^2 - h^2 = 0, \tag{40}$$

where R and h are material parameters. This model is extended by Zhang et al. (1997) to study the yielding of polymeric foams, with an added parameter to define the centre of the yield locus,

$$\frac{\left[\sigma_m - X_0(\varepsilon_{vp})\right]^2}{a(\varepsilon_{vp})} + \frac{\sigma_e^2}{b(\varepsilon_{vp})} \leqslant 1, \tag{41}$$

where ε_{vp} is the plastic volumetric strain, and $X_0(\varepsilon_{vp})$, $a(\varepsilon_{vp})$, $b(\varepsilon_{vp})$ are the material parameters to be determined from uniaxial compression, simple shear, and hydrostatic compression tests. For polymeric foams having a zero plastic Poisson's ratio (i.e., $\nu_p = 0$), a non-associated flow potential, $\Phi^* = \sigma_e^2 + (9/2)\sigma_m^2$, has been assumed.

Compared with rigid polymeric foams, the yielding of metal foams is complicated by the presence of various types of morphology imperfections (Chen et al., 1999). Although Eq. (39) suggests that the hydrostatic yield strength of a perfect foam is governed by cell-wall stretching and that its uniaxial strength is dominated by cell-wall bending, Chen et al. (1999) found that a small degree of imperfections such as cell-wall waviness and misalignment suffices to induce cell-wall bending under all macroscopic stress states, reducing the hydrostatic strength to the same level as the uniaxial strength. Combining the yield function (39) for rigid foams and the modified Mises model of Drucker and Prager (1952) for soil, Miller (2000) developed a phenomenological plastic model with three adjustable parameters to account for the different yield limits of metal foams in tension and compression and the nearly circular yield surface in the σ_e–σ_m space. Based upon the elliptical yield function (40), Deshpande and Fleck (1999) proposed two phenomenological constitutive models for metallic foams: the self-similar model and the differential hardening model. In the first model, the aspect ratio R of the ellipse is a material constant, whereas h depends not only upon the accumulated plastic strain but also upon the stress state and is characterised by the uniaxial and hydrostatic compression stress versus strain curves. The more complicated differential hardening model is developed to capture the experimentally observed evolution of shape of yield surface in metallic foams. Here, both R and h are assumed to be strain *and* stress states dependent, requiring four material parameters to characterise hardening. Although an improved accuracy is obtained by using the differential hardening model, detailed test data on the initial yield surface and its evolution must be provided to determine the four material parameters.

As was mentioned before, the present focus is placed on the constitutive modelling of the compressive behaviour of cellular metal foams. Thus, it is assumed that $\Phi_1 = C(\bar{\varepsilon})\sigma_m^2$ in Eq. (13) such that

$$\Phi = \bar{\sigma}^2 + C(\bar{\varepsilon})\sigma_m^2 - Y(\bar{\varepsilon}) = 0 \tag{42}$$

is the new stress potential for cellular foams, where $C(\bar{\varepsilon})$ and $Y(\bar{\varepsilon})$ are material properties to be evaluated by two characteristic tests. In this study, uniaxial and hydrostatic compression tests will be used. Most experimental investigations on metal foams are conducted under uniaxial loading (e.g., Thornton and Magee, 1975; Gibson and Ashby, 1997; Sugimura et al., 1997; Andrews et al., 1999; McCullough et al., 1999). Multiaxial tests are performed by Triantafillou et al. (1989) on open cell metallic foams, and by Gioux et al. (1999) and Deshpande and Fleck (1999) on open and closed metallic foams. The results of Triantafillou et al. (1989) and Gioux et al. (1999) are reported in terms of yield limits (yield surfaces) – no stress versus strain curves are given – and hence cannot be used to calibrate the stress potential (42). Stress versus strain curves under several different proportional loading paths are reported in detail by Deshpande and Fleck (1999) for a high density closed cell aluminium foam (Alporas foam from Shinko Wire Company, Japan) and for a low-density open cell aluminium foam (Duocel foam from ERG Company, USA), which are sufficient to characterise and validate the present model.

Deshpande and Fleck (1999) measured the stress versus strain curves for both Alporas foam (relative density $\rho = 0.16$) and Duocel foam ($\rho = 0.07$) under either uniaxial or hydrostatic compression loading, respectively. The resulting hydrostatic and uniaxial characteristic stress $\bar{\sigma}$ versus characteristic strain $\bar{\varepsilon}$ curves for the Alporas and Duocel foams are shown in Fig. 6, which are calculated by substituting the Deshpande–Fleck results into Eqs. (10) and (11). The subscripts 'hc' and 'uc' are used in Fig. 6 to denote hydrostatic and uniaxial compression, respectively. It is noticed that the experimental results of Deshpande and Fleck (1999) are presented in terms of stress versus plastic strain. The elastic strain is therefore assumed to be negligibly small in the present model so that the total strain ε_{ij} equals the plastic strain ε_{ij}^p. Further, Poisson's ratio v is taken to be 0.23 for the Alporas foam and 0.15 for the Duocel foam, corresponding to the plastic Poisson's ratio v_p at the lowest plastic strain level ($\sim$0.04) reported in Deshpande and Fleck (1999). The two material parameters $C(\bar{\varepsilon})$ and $Y(\bar{\varepsilon})$ in Eq. (42) for the metallic foams, determined from the hydrostatic and uniaxial characteristic stress $\bar{\sigma}$ versus characteristic strain $\bar{\varepsilon}$ curves shown in Fig. 6, are

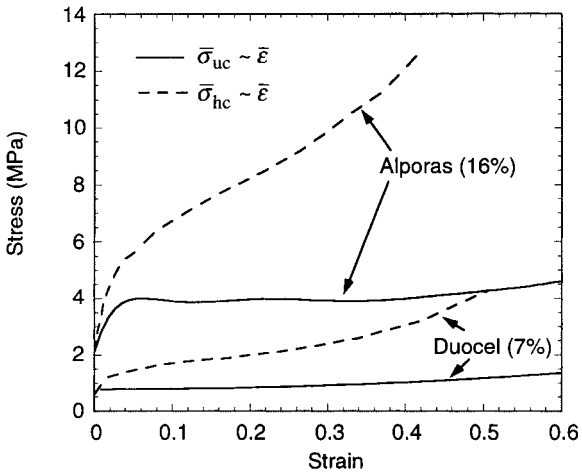

Fig. 6. Characteristic $\bar{\sigma}$–$\bar{\varepsilon}$ curves for characterising constitutive models for Alporas foam ($\rho = 0.16$) and Duocel foam ($\rho = 0.07$) under uniaxial and hydrostatic compression.

$$C(\bar{\varepsilon}) = \frac{\bar{\sigma}_{hc}^2 - \bar{\sigma}_{uc}^2}{\bar{\sigma}_{uc}^2/(9+\beta^2) - \bar{\sigma}_{hc}^2/\beta^2},$$
$$Y(\bar{\varepsilon}) = \bar{\sigma}_{hc}^2\bar{\sigma}_{uc}^2 \frac{1/(9+\beta^2) - 1/\beta^2}{\bar{\sigma}_{uc}^2/(9+\beta^2) - \bar{\sigma}_{hc}^2/\beta^2}. \tag{43}$$

Together with the associated flow rule (15) and consistence condition (16), the stress potential (42) can now be used to study the constitutive behaviour of both Alporas and Duocel foams.

Contours of the stress potential between the loading paths of uniaxial and hydrostatic compression for selected values of $\bar{\varepsilon}$ are shown in Fig. 7a for Alporas and in Fig. 7b for Duocel. Under uniaxial and hydrostatic compression, it has been established that the model reproduces, as expected from Eq. (43), the measured stress–strain curves for both Alporas and Duocel. To properly validate the constitutive model, tests other than uniaxial and hydrostatic compression are needed. The axisymmetric proportional loading

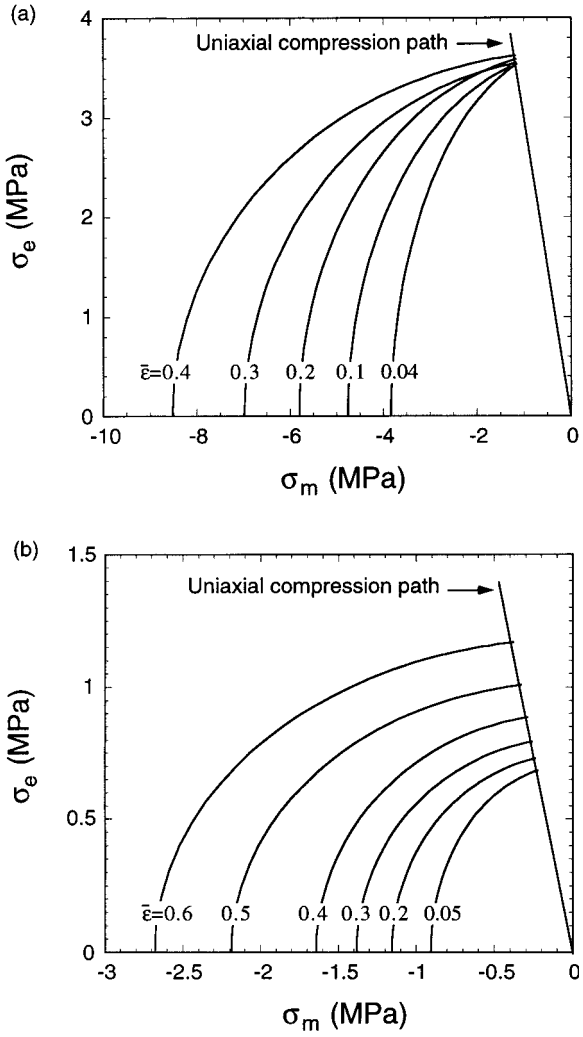

Fig. 7. Stress potential contours at selected characteristic strain levels for (a) Alporas foam, (b) Duocel foam.

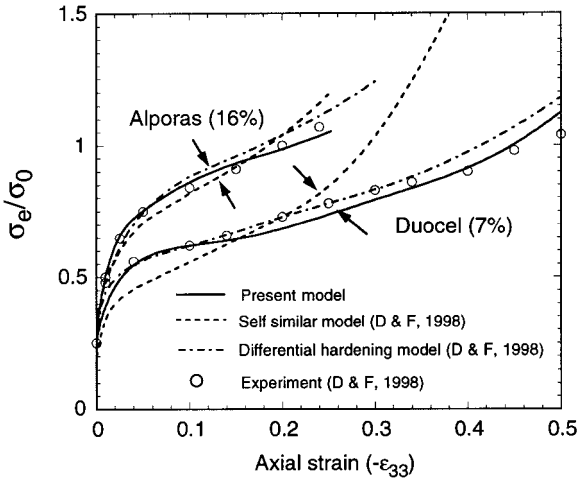

Fig. 8. Comparison between predicted and measured stress versus strain curves for Alporas and Duocel metal foams under axisymmetric proportional loading with $\eta = 3$.

path (i.e., Eq. (25) with $\sigma < 0$), which is the same path used by Deshpande and Fleck (1999) in their experiments, is selected. Following Deshpande and Fleck (1999), the stress ratio

$$\eta = -\frac{\sigma_m}{\sigma_e} \tag{44}$$

is introduced to define the direction of loading in the σ_e–σ_m space, with $\eta = 1/3$ standing for uniaxial compression and $\eta \to \infty$ for hydrostatic compression. For the particular loading path of $\eta = 3$, the stress versus strain curves predicted separately from the present model, the self-similar model and differential hardening model of Deshpande and Fleck (1999) are plotted in Fig. 8 together with those measured for Alporas and Duocel foams. In Fig. 8, the effective stress has been normalised by the uniaxial yield strength $\sigma_0 = 1.73$ MPa for the Alporas foam and $\sigma_0 = 0.5$ MPa for the Duocel foam. The present model with only two material parameters is seen to give equally accurate predictions as those from the more sophisticated differential hardening model with four adjustable parameters. It appears that the self-similar model somewhat overestimates the hardening behaviour, especially at large strain levels.

4. Concluding remarks

A simple framework of developing phenomenological constitutive models of elastoplasticity for both plastically incompressible and compressible materials is presented. A stress potential based on characteristic stress and total strain is proposed, which differs from the conventional yield function as no attempt is made to separate elastic strains from plastic deformations. The stress potential and the associated constitutive model are characterised by a set of multiaxial tests; no information about the initial yield surface and its evolution is required. In the limiting case, the three-dimensional constitutive model reduces to the classical Mises model. A two-dimensional version of the constitutive model has also been formulated. The predicted constitutive behaviours compare well against the experimental measurements for grey cast iron and two types of metallic foam, the former plastically incompressible and the latter compressible. Because the

stress–strain curves along different loading paths can be predicted fairly accurately by the proposed model, the initial yield surface and its subsequent evolution, if needed, can be easily constructed once the definition of yielding is specified.

The aim of this paper is to introduce, based on the elastic complementary energy, a pair of characteristic stress and strain suitable for capturing the elasto-plastic behaviour of solid materials, applications of the theory have focused on isotropic materials subjected to proportional loading. More complicated loading paths (e.g., non-proportional loading) require further investigation. Extending the model to cover topics such as material anisotropy and rate dependent deformation is also of interest in future work.

Acknowledgements

This work was partially supported by EPSRC, UK, and partially by the ARPA/ONR MURI program, USA, on Ultralight Metal Structures (No. N00014-1-96-1028). The authors wish to thank Profs. Norman Fleck and John W. Hutchinson for helpful discussions.

References

Ashby, M.F., Evans, A.G., Hutchinson, J.W., Fleck, N.A., 1998. Metal foams: a design guide. Technical Report CUED/C-MICROMECH/TR.3, Engineering Department, Cambridge University.

Andrews, E., Sanders, W., Gibson, L.J., 1999. Compressive and tensile behaviour of aluminium foams. Mater. Sci. Engng. A. 270, 113–124.

Barlat, F., Lege, D.J., Brem, J.C., 1991. A six-component yield function for anisotropic materials. Int. J. Plast. 7, 693–712.

Bassani, J.L., 1977. Yield characterisation of metals with transversely isotropic plastic properties. Int. J. Mech. Sci. 19, 651–660.

Chen, C., Lu, T.J., Fleck, N.A., 1999. Effect of imperfections on the yielding of two-dimensional foams. J. Mech. Phys. Solids. 47, 2235–2272.

Coffin Jr., L.F., 1950. The flow and fracture of a brittle material. ASME J. Appl. Mech. 72, 233–248.

Deshpande, V.S., Fleck, N.A., 1999. Isotropic constitutive models for metallic foams. J. Mech. Phys. Solids, submitted for publication.

Drucker, V.S., 1948. Relation of experiments to mathematical theories of plasticity. ASME J. Appl. Mech. 16, 349–357.

Drucker, D.C., Prager, W., 1952. Soil mechanics and plastic analysis or limit design. Quart. Appl. Mech. 10, 157–165.

Gibson, L.J., Ashby, M.F., 1997. Cellular Solids: Structure and Properties, second ed. Cambridge University Press, Cambridge, UK.

Gibson, L.J., Ashby, M.F., Zhang, J., Triantafillou, T.C., 1989. Failure surfaces for cellular materials under multiaxial loads – I. Modeling. Int. J. Mech. Sci. 31, 635–663.

Gioux, G., McCormack, T.M., Gibson, L.J., 1999. Failure of aluminium foams under multiaxial loads. Int. J. Mech. Sci., submitted for publication.

Hecker, S.S., 1975. Experimental studies of yield phenomena in biaxially loaded metals. In: Constitutive equations in viscoplasticity: computational and engineering aspect, ASME, AMD, 20, 1–33.

Hill, R., 1950. Mathematical Theory of Plasticity. Oxford University Press, Oxford, UK.

Hill, R., 1994. Classical plasticity: a retrospective view and a new proposal. J. Mech. Phys. Solids 42, 1803–1816.

Hjelm, H.E., 1994. Yield surface for grey cast iron under biaxial stress. ASME J. Engng. Mater. Tech. 116, 148–154.

Karafillis, A.P., Boyce, M.C., 1993. A general anisotropic yield criterion using bounds and a transformation weighting tensor. J. Mech. Phys. Solids 41, 1859–1886.

McCullough, K.Y.G., Fleck, N.A., Ashby, M.F., 1999. Uniaxial stress–strain behaviour of aluminium alloy foams. Acta Mater. 47, 2323–2330.

Miller, R.E., 2000. A continuum plasticity model of the constitutive and indentation behaviour of foamed metals. Int. J. Mech. Sci. 42, 729–754.

Puso, M.A., Govindjee, S., 1995. Phenomenological constitutive model for rigid polymeric foam. ASME MD 68, 159–176.

Sugimura, Y., Meyer, J., He, M.Y., Bart-Smith, H., Grenestedt, J.L., Evans, A.G., 1997. On the mechanical performance of closed cell Al alloy foams. Acta Mater. 45, 5345–5359.

Takeda, T., 1993. Yield and flow behaviour of initially anisotropic aluminium tube under multiaxial stresses. ASME J. Engng. Mater. Tech. 115, 77–82.

Thornton, P.H., Magee, C.L., 1975. The deformation of aluminium foams. Met. Trans. 6A, 1253–1263.

Triantafillou, T.C., Zhang, J., Shercliff, T.L., Gibson, L.J., Ashby, M.F., 1989. Failure surfaces for cellular materials under multiaxial loads – II. Comparison of models with experiment. Int. J. Mech. Sci. 31, 665–678.

Warren, W.E., Kraynik, A.M., 1987. Foam mechanics: the linear elastic response of two-dimensional spatially periodic cellular materials. Mech. Mater. 6, 27–37.

Zhang, J., Lin, Z., Wong, A., Kikuchi, N., Li, V.C., Yee, A.F., Nusholtz, G.S., 1997. Constitutive modeling and material characterisation of polymeric foams. ASME J. Engng. Mater. Tech. 119, 284–291.